Low-Temperature Catalytic NO Reduction with CO by Subnanometric Pt Clusters

Estefanía Fernández,[†,⊥] Lichen Liu,[†,⊥] Mercedes Boronat,[†] Raul Arenal,[‡,§,‖] Patricia Concepcion,[†] and Avelino Corma*,[†]

[†]Instituto de Tecnología Química, Universitat Politècnica de València-Consejo Superior de Investigaciones Científicas (UPV-CSIC), Av. de los Naranjos s/n, 46022 Valencia, Spain

[‡]Laboratorio de Microscopias Avanzadas, Instituto de Nanociencia de Aragon, Universidad de Zaragoza, Mariano Esquillor Edificio I + D, 50018 Zaragoza, Spain

[§]ARAID Foundation, 50018 Zaragoza, Spain

[‖]Instituto de Ciencias de Materiales de Aragon, CSIC-Universidad de Zaragoza, C/Pedro Cerbuna 12, 50009 Zaragoza, Spain

S *Supporting Information*

ABSTRACT: The catalytic subnanometric metal clusters with a few atoms can be regarded as an intermediate state between single atoms and metal nanoparticles (>1 nm). Their molecule-like electronic structures and flexible geometric structures bring rich chemistry and also a different catalytic behavior, in comparison with the single-atom or nanoparticulate counterparts. In this work, by combination of operando IR spectroscopy techniques and electronic structure calculations, we will show a comparative study on Pt catalysts for CO + NO reaction at a very low temperature range (140−200 K). It has been found that single Pt atoms immobilized on MCM-22 zeolite are not stable under reaction conditions and agglomerate into Pt nanoclusters and particles, which are the working active sites for CO + NO reaction. In the case of the catalyst containing Pt nanoparticles (∼2 nm), the oxidation of CO to CO_2 occurs in a much lower extension, and Pt nanoparticles become poisoned under reaction conditions because of a strong interaction with CO and NO. Therefore, only subnanometric Pt clusters allow NO dissociation at a low temperature and CO oxidation to occur well on the surface, while CO interaction is weak enough to avoid catalyst poisoning, resulting in a good balance to achieve enhanced catalytic performance.

KEYWORDS: *single atoms, subnanometric metal clusters, platinum, CO + NO, operando IR, DFT calculations*
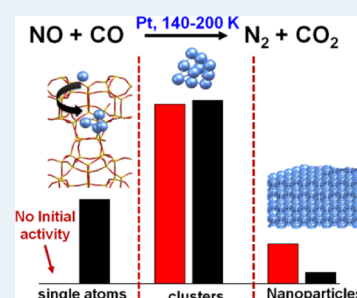
INTRODUCTION

In the last years, the recognition of extremely high reactivity associated with single metal atoms and/or clusters of low atomicity has open great expectation in "nano" catalysis, specifically focused in the subnanometer level.[1,2] The unique geometric and electronic structures of the subnanometric metal catalysts can invoke distinct catalytic properties compared to conventional nanoparticulate metal catalysts.[3]

For instance, small Au clusters with less than 10 atoms have been identified as the catalytically active species in CO,[4,5] alkane, and thiol oxidation reactions.[6,7] Ag_3 clusters supported on Al_2O_3 catalyze the epoxidation of propene with O_2 with high activity and selectivity at a low temperature,[8] while subnanometric Cu clusters have been reported to be highly active for the reduction of CO_2 with H_2 to methanol[9] and for the oxidation of CO with N_2O.[10] Nevertheless, subnanometric Pt species have been demonstrated as highly active sites in several catalytic processes, like CO oxidation, water−gas shift reaction, and the oxidative dehydrogenation of alkanes.[11−13] In addition, recently, subnanometric Pd_n clusters with $n < 20$ have shown enhanced catalytic activity in the CO + NO reaction compared to larger particles and single crystals.[14,15]

Fundamental understanding of those size effects at a molecular level has been mainly achieved by electronic structure calculations and surface science studies.[16−18] On the other hand, corresponding studies on size-selected real catalysts have been very scarce because of the sophisticated catalyst preparation methods needed for controlling metal cluster atomicity and the lack of characterization methods enabling resolution at a molecular and atomic level. Recently, our group has succeeded in the preparation of Au and Pt clusters of low atomicity stabilized inside pure-silica zeolite,[19,20] which opens the possibility to explore those catalysts for potential industrial applications, for instance, aerobic oxidation of cyclohexane to cyclohexanol and cyclohexanone and propane dehydrogenation to propylene. By in situ transmission electron microscopy and IR spectroscopy, we have also observed the relevance of dynamic structural transformation of subnanometric Pt species under reaction conditions.[21]
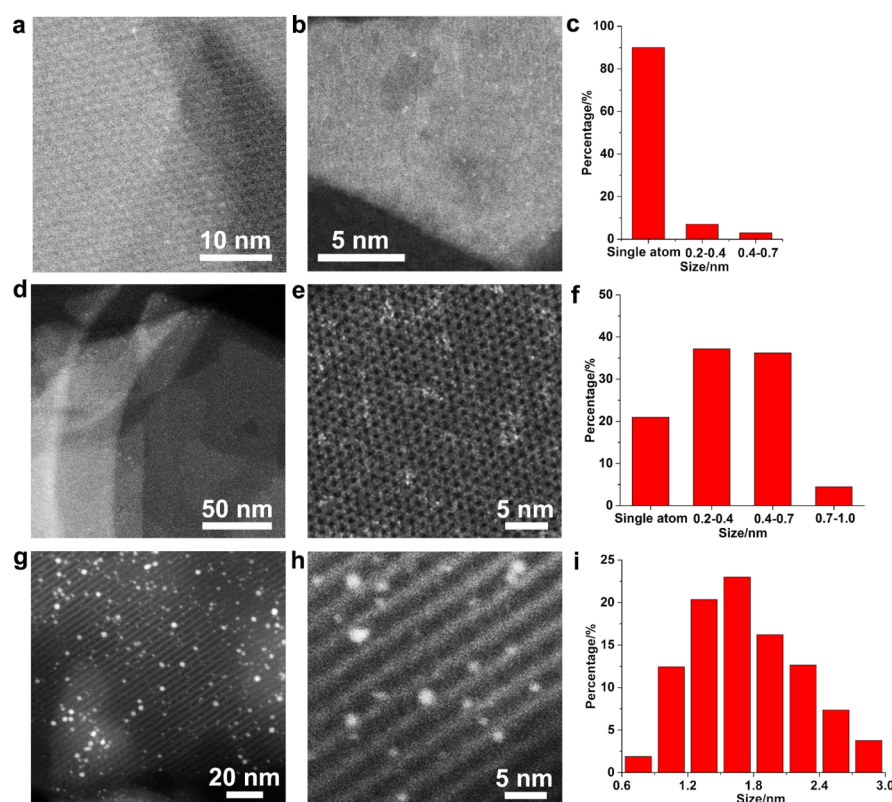
Figure 1. Morphological characterizations of Pt-SA, Pt-CL, and Pt-NP. (a,b) STEM images of the Pt-SA sample, showing the presence of single Pt atoms dispersed on MCM-22. (d,e) STEM images of the Pt-CL sample, showing the presence of subnanometric Pt clusters and small fraction of Pt single atoms. (g,h) STEM images of the Pt-NP sample, showing the presence of Pt nanoparticles dispersed in the mesoporous channels and on the surface of MCM-41. Size distributions of Pt species in Pt-SA, Pt-CL, and Pt-NP are shown in (c,f,i), respectively.

In the present study, it will be shown that it is possible to catalyze the reaction between CO and NO at a temperature as low as 140 K with subnanometric Pt clusters stabilized in the pores of zeolite, while Pt single atoms are inactive. Spectroscopic studies under operando conditions and electronic structure calculations have allowed the explanation of the enhanced catalytic activity observed on Pt clusters at such low temperature values. Notably, NO dissociation is observed on subnanometric Pt clusters at 140 K, which usually occurs above 473 K.[22,23] The unique reactivity of subnanometric Pt clusters can be understood by the fast reaction of the O atoms formed by NO dissociation with CO to produce CO_2. In the case of Pt NP, the strong CO adsorption limits the extension of CO oxidation to CO_2, while in the case of a Pt single atom, fast sintering to the Pt cluster under reaction conditions is observed.

■ RESULTS AND DISCUSSION

Catalyst Preparation and Structure Characterization. Subnanometric Pt species, including single Pt atoms (Pt-SA) and Pt clusters (Pt-CL) confined in MCM-22 zeolite, were synthesized following a new strategy,[19] where the 12 ring "cups" (~0.7 nm) on the surface and the internal supercages (~0.7 × 1.8 nm) can stabilize those Pt species.[24] A different material containing larger Pt nanoparticles supported on mesoporous MCM-41 (Pt-NP sample) was synthesized by conventional wetness impregnation, as described in the Experimental Section. The three samples were characterized by high-angle annular dark-field high-resolution scanning transmission electron microscopy imaging (HAADF-HRSTEM

imaging). The Pt-SA sample mostly contains Pt single atoms together with a small fraction of Pt clusters with the particle diameter below 0.7 nm (Figure 1a−c). In the Pt-CL sample, subnanometric Pt clusters with the diameter between 0.2 and 0.7 nm were mainly observed, as well as a few Pt single atoms (Figure 1d−f). An average atomicity of 13 atoms was determined by extended X-ray absorption fine structure spectroscopy performed on this sample, as presented in our previous work.[19] Finally, Pt nanoparticles with the diameter ranging from 0.7 to 3.0 nm and an average particle size of 2.0 nm were observed in the Pt-NP sample (Figure 1g−i). According to the above structural characterizations, these three Pt samples can be suitable model catalysts for performing a comparative study on the catalytic behavior of single Pt atoms, Pt clusters, and nanoparticles.

Catalytic Studies with Combined Infrared-Mass Spectrometry. The catalytic performance of the three Pt samples in the CO + NO reaction was followed by mass spectrometry (MS) using a coupled IR-MS system that allows to obtain information of adsorbed species from the IR spectra acquired under operando conditions and, simultaneously, to analyze catalyst reactivity (see the experimental details in the Supporting Information). In order to get information about the elementary reaction steps taking place on the catalyst surface, studies at low surface coverage (0.3−2.8%) have been performed. Isotopically labeled ^{13}CO and ^{15}NO were used as the reactants for identification of reaction products based on their mass signals. The production of $^{13}CO_2$ and $^{15}N_2$ at 140 and 200 K on Pt-SA, Pt-CL, and Pt-NP samples under stream

conditions are plotted in Figure S1a−c and summarized in Table 1.

Table 1. $^{13}CO_2$ and $^{15}N_2$ Formation[a] at 140 and 200 K on Pt-CL, Pt-NP, and Pt-SA Samples

temperature	TOF[a] Pt-CL ($\times 10^5$)		TOF[a] Pt-NP ($\times 10^5$)		TOF[a] Pt-SA ($\times 10^5$)	
	$^{13}CO_2$	$^{15}N_2$	$^{13}CO_2$	$^{15}N_2$	$^{13}CO_2$	$^{15}N_2$
140 K	1.96[b]	0.47[b]	0.18[d]	0.27[d]		
200 K	5[c]	0.54[c]	0.34[e]	0.43[e]	2.06[f]	0.53[f]

[a]Turnover frequency (TOF) measured as mol_{CO_2} s^{-1} mol_{Pt}^{-1} and mol_{N_2} s^{-1} mol_{Pt}^{-1}. [b]Reactivity for low temperature NO + CO reaction measured at 450 s of reaction at 140 K. [c]Reactivity for low temperature NO + CO reaction at 670 s of reaction at 200 K. [d]Reactivity for low temperature NO + CO reaction at 1200 s of reaction at 140 K. [e]Reactivity for low temperature NO + CO reaction at 1500 s of reaction at 200 K. [f]Reactivity for low temperature NO + CO reaction at 800 s of reaction at 200 K.

The Pt-SA sample was initially inactive at 200 K (Figure S1a). $^{13}CO_2$ production was started to be observed after 172 s, increasing slowly with reaction time. $^{15}N_2$ formation was only detected in very low amounts at ∼623 s. The ex situ TEM experiments after the CO + NO reaction on the Pt-SA sample show that agglomeration of Pt single atoms occurs, and after 850 s of reaction at 200 K, subnanometric Pt clusters and Pt nanoparticles around 1 nm are formed (Figure S2). For the Pt-CL sample (Figure S1b), $^{13}CO_2$ was formed from the beginning of the reaction at both 140 and 200 K and its production remains stable with time, while $^{15}N_2$ evolution appeared delayed (between 313 and 490 s). Gas-phase production of $^{15}N_2$ was below the stoichiometric value of 0.5 (i.e., $^{15}N_2/^{13}CO_2 \approx 0.2$) at both the temperature values. In contrast, on the Pt-NP sample (Figure S1c), both $^{13}CO_2$ and $^{15}N_2$ were already detected in the first instance of the reaction; while in this case, the $^{15}N_2/^{13}CO_2$ ratio in the products was ∼1.5. At 200 K, $^{13}CO_2$ formation rate decreased until reaching a constant value. The HAADF-HRSTEM images confirmed that no obvious sintering of Pt species under the present reaction conditions occurred on either the Pt-CL or the Pt-NP sample (see Figures S3 and S4).

$^{13}CO_2$ production rates on the three samples at 200 K at the initial reaction time (∼100 s, in red) and after 700 s of reaction (in black) were plotted together in Figure 2. Pt-CL was initially
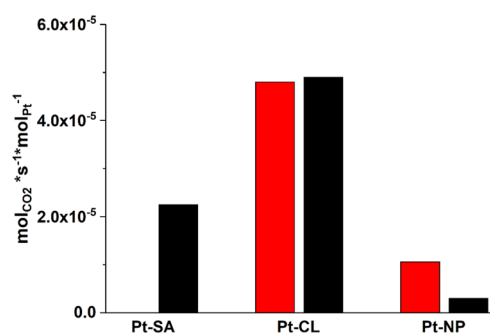

Figure 2. Activity of Pt catalysts for low-temperature NO reduction by CO. Initial $^{13}CO_2$ production rate (red bars) and reaction rate after 700 s of time on stream (black bars) at 200 K. The Pt-SA sample was inactive initially and its activity for CO_2 production increases with time on stream.

almost 4-fold more active toward $^{13}CO_2$ formation than the Pt-NP sample. On the other hand, no activity was observed on the Pt-SA sample at the beginning of the reaction, but after 700 s, its $^{13}CO_2$ production was close to that of Pt-CL.

To get a better understanding of the catalytic behavior of different Pt entities at low temperature, the IR spectra of the three samples acquired under operando conditions at 140 and 200 K were analyzed in detail (Figure 3a−c). The Fourier transform infrared spectra of the MCM-22 sample without Pt in the presence of $^{15}NO + ^{13}CO$ at 140 K is shown in Figure S5. IR bands at ∼2284 and 2166 cm^{-1} correspond to $^{13}CO_2$ and $^{15}N_2O$, respectively, while bands at 2105 and 2092 cm^{-1} can be associated to ^{13}CO adsorbed on Si−OH groups. Moreover, IR bands associated to $^{15}N_2O_3$ (at 1836 and 1815 cm^{-1}), $^{15}N_2O_4$ (at 1700 cm^{-1}) and nitrates (bands in the 1576−1554 cm^{-1} range) were also observed.[25] In agreement with previous work,[26] some NO oxidation may take place inside the pores of MCM-22, but at a very low extension, because none of these species was detected in the gas phase by an on-line mass spectrometer. Moreover, the lack of $^{13}CO_2$ and $^{15}N_2$ in the effluent gas stream confirms the irrelevant role of the MCM-22 zeolite for the catalytic CO + NO reaction when working at ≤200 K.

In the case of the Pt-NP sample (Figure 3), besides the IR bands already detected in the MCM-22 sample, additional bands related to ^{13}CO and ^{15}NO bonded to platinum surface species were observed. In particular, at 140 K, IR bands at 2281 and 2160 cm^{-1} can be ascribed to $^{13}CO_2$ and $^{15}N_2O$, respectively. Besides, ^{13}CO bonded to Si−OH (2108 cm^{-1}) and ^{13}CO bonded to $Pt^{\delta+}$ (2088 cm^{-1}) and Pt^0 (2043 cm^{-1}) were also observed (see Figure 3a,b).[27] Several types of NO_x species can be observed in the IR spectra, including ^{15}NO bonded to Pt^0 surface sites (1850 cm^{-1}),[28] $^{15}N_2O_4$ (1710 cm^{-1}), and nitrates (1553 cm^{-1}). Because the sample was reduced in the IR cell before the introduction of ^{13}CO and ^{15}NO, the presence of $Pt^{\delta+}$ should come from ^{15}NO dissociation on Pt nanoparticles, where the resultant oxygen atom on the partially oxidized Pt surface would further react with ^{13}CO to form $^{13}CO_2$. When increasing the reaction temperature from 140 to 200 K (see Figure 3c,d), ^{13}CO adsorbed on $Pt^{\delta+}$ species is not observed anymore and the IR bands at 2045 and 1850 cm^{-1} correspond to ^{13}CO and ^{15}NO adsorbed on Pt^0, respectively.

Based on the IR spectra acquired on Pt-NP under operando conditions, it can be concluded that Pt NPs are partially oxidized by ^{15}NO at 140 K resulting in $Pt^{\delta+}$, and the surface of the Pt nanoparticles are covered by strongly adsorbed ^{13}CO and ^{15}NO species at both 140 and 200 K. As a consequence of surface oxidation by NO and the blocking effect from $^{13}CO/^{15}NO$ adsorption, the amount of surface metallic Pt sites available for NO dissociation (which has been reported as active sites for NO dissociation,[23,29,30]) strongly decreases, resulting in a low catalytic activity, in agreement with previous studies.[31,32]

In the case of Pt-CL, the IR spectra recorded under operando conditions are similar to those observed in the Pt-free MCM-22 reference sample (Figure S6). However, in contrary to the Pt-NP sample, IR bands associated to Pt interacting with ^{13}CO and ^{15}NO species are not observed, indicating either a weak interaction of these molecules with Pt surface sites or a fast reaction toward the production of $^{13}CO_2$ and $^{15}N_2$. Because both $^{13}CO_2$ and $^{15}N_2$ were detected in the
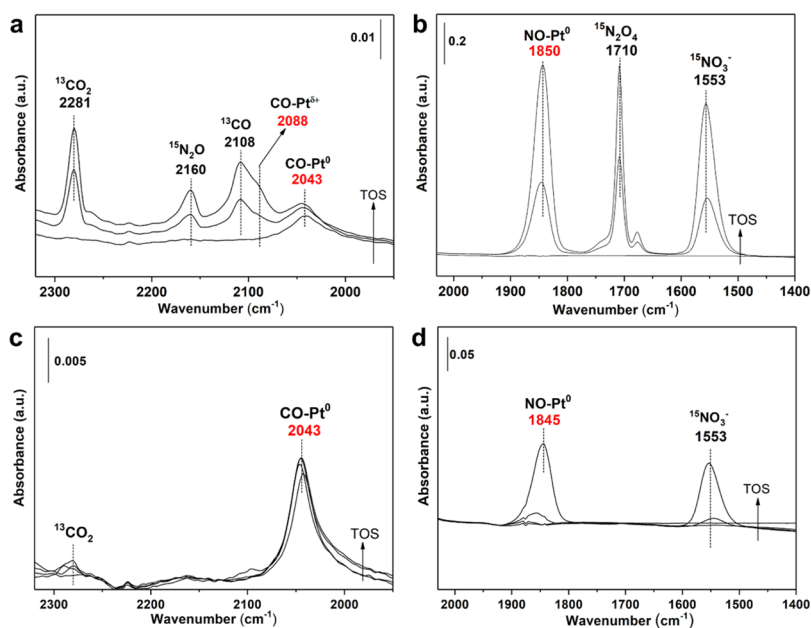
Figure 3. IR spectra in the (2320−1950) cm^{-1} IR region and (2030−1400) cm^{-1} IR region of the Pt-NP sample in the presence of $^{13}CO + ^{15}NO$ at 140 K (a,b) and 200 K (c,d). Spectra have been acquired at different reaction times (TOS), that is, 180, 780, and 1500 s (a,b); and 240, 600, and 2100 s (c,d).
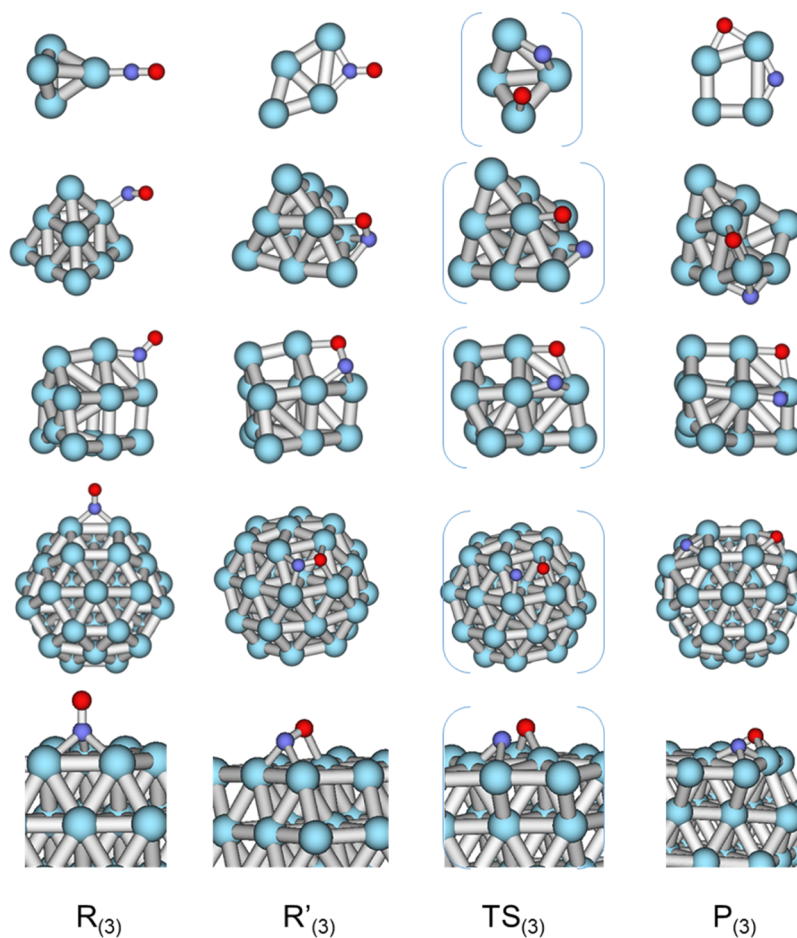
Figure 4. Optimized structures of reactant R, transition state TS, and product P involved in the lowest energy pathways for NO dissociation (step 3) over Pt_4, Pt_{10}, Pt_{13}, and Pt_{38} and Pt(111) catalyst models. Pt, N, and O atoms are depicted as light blue, dark blue, and red balls, respectively.

effluent gas by a mass spectrometer, a high reactivity of Pt-CL in the CO + NO reaction is proposed. In order to study the

chemical state of the Pt clusters under working conditions, the Pt-CL sample was titrated using CO as the probe molecule

Table 2. Activation (E_{act}) Energies (in kcal mol^{-1}) for All Elementary Steps in the Mechanism of CO + NO Reaction Over Pt Clusters and Nanoparticles, Calculated as $E_{act} = E(TS) - E(R)$ Except the Values in Parenthesis Which are Calculated as $E_{act} = E(TS) - E(R')$[a]

step		Pt_4	Pt_{10}	Pt_{13}	Pt_{38}	$Pt(111)$
NO* → N* + O*	(3)	69.3 (52.5)	45.2 (24.4)	33.7 (9.1)	20.6 (7.1)	52.3 (39.7)
CO* + O* → CO$_2$	(4)	19.4	19.8	13.3	16.8	18.0
2N* → N$_2$	(5)	29.3 (22.2)	37.2 (27.2)	28.4 (22.0)	38.1 (5.8)	52.9 (21.5)
2N* → N$_2$ (high N*)	(5)			19.8	4.8	37.9
NO* + CO* → N* + CO$_2$	(6)	79.6	47.7	49.7	54.2	39.0
N* + CO* → NCO*	(7)	34.4 (29.8)	42.0	28.6	38.2 (24.9)	
N* + NO* → N$_2$O*	(8)	43.2 (25.1)	27.7	32.7 (19.1)	23.5 (22.5)	
N$_2$O* + CO* → N$_2$ + CO$_2$	(9)	33.1	33.1	33.8	26.8	

[a]The structures involved are depicted in Figures 4, 5, S16, S17, S19, S21−S24.

after catalytic reaction at 200 K. As shown in Figure S7, Pt^0 species (IR band at 2040 cm^{-1}) were detected, indicating that Pt clusters remain in an active metallic state under reaction conditions, while the oxygen resulting from ^{15}NO dissociation is transferred to ^{13}CO to produce ^{13}CO$_2$. In contrast to the Pt-NP sample, subnanometric Pt clusters in the Pt-CL sample are less prone to become oxidized at a low temperature because of the fast reaction between ^{13}CO and the oxygen species generated from ^{15}NO dissociation.

Finally, in the case of the Pt-SA sample, IR bands at 2054 and 2076 cm^{-1} associated to ^{13}CO−Pt^0 and ^{13}CO−Pt$^{\delta+}$, respectively, are observed in the operando IR spectra at 200 K (Figure S8), which is similar to the situation observed in the Pt-NP sample. This reflects a sintering of single atoms toward Pt nanoparticles during the reaction, as confirmed from the HAADF-HRSTEM images shown in Figure S2.
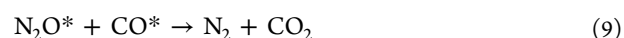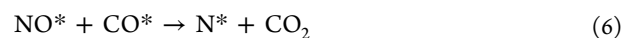
To summarize the results from operando IR studies, it is clear that regardless of whether the reaction occurs on Pt clusters or Pt nanoparticles, ^{15}NO dissociation can occur at a low temperature (140−200 K), leading to the formation of O species on the surface of Pt. However, while the O species on Pt clusters react fast with ^{13}CO to form CO$_2$ and to maintain the Pt clusters in the metallic state, the much stronger interaction of CO with the Pt atoms in the Pt nanoparticles decreases the rate of the CO + O reaction, resulting in partial oxidation of the nanoparticles. Therefore, the low temperature CO + NO reaction can proceed smoothly on Pt clusters while Pt nanoparticles show lower activity.

Computational Studies. To understand the reaction mechanism of low-temperature CO + NO reaction on Pt species with different particle sizes, density functional theory (DFT) calculations with four clusters of different atomicity, Pt_4, Pt_{10}, Pt_{13}, and Pt_{38}, were considered, together with a periodic model for a Pt atom placed in the cavity of MCM-22, and a slab model of the Pt(111) surface to represent large nanoparticles (see Figures 4 and S9). The zeolite support was considered in the model of the Pt atom to confirm, as will be discussed later, that isolated Pt atoms in MCM-22 zeolite are not stable under reaction conditions and sinter forming clusters. Then, to analyze the influence of cluster atomicity on the bond-breaking and bond-forming steps of the mechanism, which take place when the molecules are already adsorbed on the Pt clusters, the zeolite support was not considered necessary.

The following elementary steps in the mechanism of the CO + NO reaction were considered

$$NO \rightarrow NO* \tag{1}$$

$$CO \rightarrow CO* \tag{2}$$

$$NO* \rightarrow N* + O* \tag{3}$$

$$O* + CO* \rightarrow CO_2 \tag{4}$$

$$2N* \rightarrow N_2 \tag{5}$$

Equations 1 and 2 refer to the adsorption of reactants and (3) is the dissociation of NO yielding atomic species. Equation 4 represents the reaction of CO with atomic O forming the CO$_2$ product, and (5) corresponds to the recombination of atomic N forming N$_2$. In addition, alternative pathways in which NO and CO react molecularly (6), or in which atomic N* reacts with CO to form NCO (7) or with NO to form N$_2$O (8) that subsequently reacts with CO yielding the N$_2$ and CO$_2$ products (9) were computationally investigated over each of the catalyst models, and only the most relevant results are described in detail.

$$NO* + CO* \rightarrow N* + CO_2 \tag{6}$$

$$N* + CO \rightarrow NCO* \tag{7}$$

$$N* + NO \rightarrow N_2O* \tag{8}$$

$$N_2O* + CO* \rightarrow N_2 + CO_2 \tag{9}$$

Adsorption of only one CO or NO molecule on a Pt atom stabilized in the MCM-22 zeolite model is clearly exothermic, with calculated adsorption energies of −95 and −79 kcal mol^{-1}, respectively, and lead to the formation of a complex with a linear arrangement of the framework O, the Pt atom, and the C or N atom in CO or NO molecules (see Figure S9). However, co-adsorption of two molecules on the same Pt atom, forming di-carbonyl, di-nitrosyl, or a Pt−CO−NO complex, would weaken the interaction between the Pt atom and the framework O atoms. As a result, the linear unit containing the Pt atom and the CO and NO molecules would move to the center of the cavity of MCM-22. Aggregation of two such units is clearly exothermic and would explain the formation of clusters observed by STEM in the Pt-SA sample under reaction conditions. On the other hand, the products of NO dissociation over a Pt atom in MCM-22 zeolite are more than 60 kcal mol^{-1} higher in energy than the corresponding initial reactant, which would explain the initial lack of activity of the Pt-SA sample and confirm the previous hypothesis that Pt nanoclusters formed by agglomeration of Pt atoms are the working active species for the low-temperature CO + NO reaction.

In the case of subnanometric Pt clusters and Pt nanoparticles, CO preferentially adsorbs on top of low coordinated

Table 3. Reaction (E_{rea}) Energies (in kcal mol^{-1}) for all Elementary Steps in the Mechanism of CO + NO Reaction Over Pt Clusters and Nanoparticles, Calculated as $E_{rea} = E(P) - E(R)$[a]

step		Pt$_4$	Pt$_{10}$	Pt$_{13}$	Pt$_{38}$	Pt(111)
NO* → N* + O*	(3)	17.4	4.6	15.7	−9.3	6.3
CO* + O* → CO$_2$	(4)	−0.3	0.4	−2.2	3.1	−15.4
2N* → N$_2$	(5)	−33.4	−44.6	−41.0	−10.3	−21.3
2N* → N$_2$ (high N*)	(5)			−71.9	−80.1	−104.1
NO* + CO* → N* + CO$_2$	(6)	48.8	18.5	23.2	3.3	0.6
N* + CO* → NCO*	(7)	1.5	11.4	9.1	20.0	
N* + NO* → N$_2$O*	(8)	32.3	−2.9	17.6	15.4	
N$_2$O* + CO* → N$_2$ + CO$_2$	(9)	−45.0	−30.9	−37.6	−35.8	

[a]The structures involved are depicted in Figures 4, 5, S16, S17, S19, S21−S24.

Pt atoms or in bridge positions between two Pt atoms, in agreement with previous studies,[33−36] while NO forms a larger variety of complexes, as shown in Figures S10−S14 in the Supporting Information. However, only some of these adsorption complexes, in particular, bidentate species in which both N and O atoms are directly coordinated to Pt, lead to an adequate activation of the NO molecule and its dissociation. The optimized structures of reactant R$_{(3)}$, transition state TS$_{(3)}$, and product P$_{(3)}$ involved in the unimolecular dissociation of NO over Pt clusters and nanoparticles are depicted in Figure 4, with the corresponding activation and reaction energies being summarized in Tables 2 and 3.

While in the most stable adsorption modes, NO interacts with Pt only through the N atom forming one, two, or three Pt−N bonds (structures R$_{(3)}$ in Figure 4), consistent with previous studies,[34,36−40] less stable conformations (structures R′$_{(3)}$ in Figure 4) in which O also interacts with Pt are always involved in the pathways for N−O bond dissociation. Such adsorption modes facilitate the transfer of electron density from the metal to the antibonding $2\pi^*$ orbital of NO, thus weakening the N−O bond and producing an elongation of the optimized NO distance from 1.17 Å in the gas phase to 1.21, 1.29, 1.32, and 1.34 and 1.25 Å on Pt$_4$, Pt$_{10}$, Pt$_{13}$, and Pt$_{38}$, and Pt(111) models, respectively. In fact, an excellent linear correlation is obtained when activation energies for NO dissociation versus optimized NO distance in reactant structure R′$_{(3)}$ are plotted (Figure S15). Moreover, in this conformation, both O and N atoms are stabilized by the Pt surface in the transition states TS$_{(3)}$. Altogether, low activation energy barriers are obtained for Pt$_{13}$ and Pt$_{38}$ clusters when calculated with respect to R′$_{(3)}$ (E_{act} values in parenthesis in Table 2), while significantly higher values are found both on too small Pt$_4$ clusters and on the Pt(111) surface. Previous computational studies using Pt(100) and the stepped Pt(211), Pt(410), or Pt(533) surfaces as catalyst models have shown that NO decomposition is favored not only by the presence of defects but also especially by the local arrangement of the Pt atoms at the defect sites.[32,37,41] The highest reactivity was obtained on ensembles of four Pt atoms forming a square, an arrangement equivalent to that present in the Pt$_{38}$ model that also leads to the lowest activation energy in the present work. The catalytic activity observed in the Pt-NP sample (see Figure 2) can probably be attributed to step defects on the surface.

It should be noted that when the E_{act} values are calculated with respect to the most stable adsorption complex R$_{(3)}$, (values in Table 2) the trend in the activation energies does not change, and intermediate Pt$_{13}$ and Pt$_{38}$ clusters are the most reactive. This trend is in excellent agreement with the IR

operando results showing faster ^{15}NO decomposition on Pt-CL as compared to Pt-NP. The reaction energies calculated with respect to the most stable R$_{(3)}$ system (E_{rea} values in Table 3) indicate that this step is exothermic only for Pt$_{38}$ and slightly endothermic for Pt$_{10}$ and the Pt(111) surface model.

The second elementary step in the mechanism is the reaction of CO with adsorbed O atoms to form CO$_2$, step (4). In the reactant structure R$_{(4)}$, (see Figure 5 for all steps in the Pt$_{13}$ cluster and Figure S16 for step 4 in all the catalyst models) CO adsorbs on a Pt atom close to an O atom that adopts bridge positions in the smaller clusters and prefers tri-coordinated sites with increasing particle size, consistent with previous studies.[33,35,42,43] Then, through a transition state structure TS$_{(4)}$, in which the O atom breaks one of the bonds with Pt while forms a new one with C, the product P$_{(4)}$ corresponding to a bent CO$_2$ molecule with a strong C−Pt bond is obtained. The activation energies, between 13 and 20 kcal mol^{-1}, are lower than those previously obtained for NO dissociation (Table 2), indicating that the reaction of CO with adsorbed O is not the rate-determining step of the process. The calculated reaction energies indicate that this step is almost thermoneutral for all Pt catalyst models considered (Table 3).

An alternative pathway involving the direct reaction of co-adsorbed NO and CO to produce, in one step, CO$_2$ and atomic N was also considered, as described in step (6). Starting from one CO and one NO molecule adsorbed close in stable conformations (structures labelled R$_{(6)}$ in Figures 5 and S17), transition states TS$_{(6)}$ were obtained in which the O atom of NO attacks the C atom of CO, forming a N−O−C−O system with strong interaction with Pt. The activation barriers for this processes are high, being close to 80 kcal mol^{-1} on the smallest Pt$_4$ cluster, around 50 kcal mol^{-1} on the rest of the clusters, and almost 40 kcal mol^{-1} on the Pt(111) model (Table 2). The calculated reaction energies indicate that this step becomes more thermodynamically favorable as the Pt particle size increases. In any case, except for the perfect Pt(111) surface, the calculated activation energies for step (6) are clearly higher than those previously obtained for the monomolecular NO dissociation according to (3), especially for Pt$_{13}$ and Pt$_{38}$ clusters, suggesting a low contribution of the bimolecular pathway to the activation and dissociation of NO over Pt catalysts.

To further clarify this point, the following experiments were performed in our coupled IR-MS system. Pt-CL and Pt-NP samples were exposed to ^{15}NO at 140 K for 30 min, followed by evacuation at 10^{-5} mbar and annealing in vacuum at 213 K, until no IR bands associated with any adsorbed ^{15}NO species were observed in the IR spectra. Then, the samples were
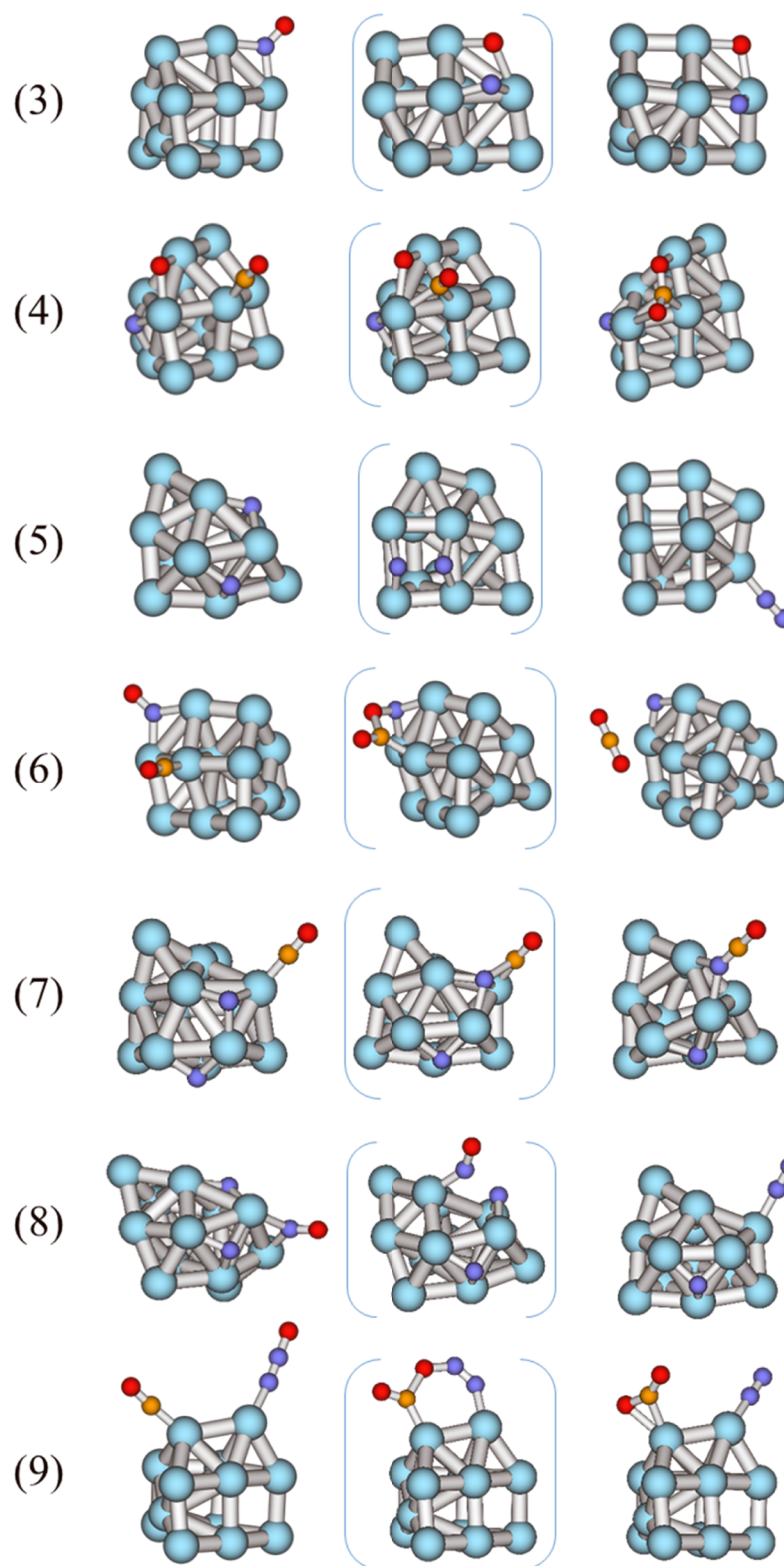
Figure 5. Optimized structures of reactant R, transition state TS, and product P for all the elementary steps (3)−(9) of the NO + CO reaction mechanism over the Pt$_{13}$ cluster model. Pt, N, C, and O atoms are depicted as light blue, dark blue, orange, and red balls, respectively.

cooled down to 140 K and subsequently exposed to ^{13}CO. As clearly seen in Figure S18, ^{13}CO$_2$ was immediately formed on both Pt-CL and Pt-NP samples, thus demonstrating that the presence of adsorbed O atoms unambiguously arises from ^{15}NO dissociation and can further react with ^{13}CO to form ^{13}CO$_2$. These experiments confirm, on the one hand, the

contribution of the NO dissociative pathway in the reaction mechanism and, on the other hand, that reaction of ^{13}CO with atomic O to form ^{13}CO$_2$ is not the rate-determining step in the global reaction mechanism. Moreover, ^{13}CO$_2$ formation on the Pt-NP sample was found to be ∼5-fold lower than on the Pt-CL sample, indicating a lower concentration of adsorbed O

atoms on the Pt-NP, in agreement with the higher activation barrier for NO dissociation obtained on the Pt(111) model. To our knowledge, this is the first time where NO dissociation at such a low temperature has been directly observed on metal catalysts.

The last step in the global mechanism is the recombination of two adsorbed N atoms to form N_2 and then desorption from the catalyst, as described by eq 5. The optimized structures of the species involved in this elementary step are depicted in Figures 5 and S19. In all the cases, N atoms preferentially occupy distant 3-fold positions (bridge in the case of Pt_4) on the Pt cluster or nanoparticle surface, structures labelled $R_{(5)}$, and they have to become closer and move to bridge positions, structures labelled $R'_{(5)}$, in order to start the recombination process. The calculated activation energy over the smallest Pt_4 cluster is much lower than that found for NO dissociation, step (3), no matter whether it is related to minimum $R_{(5)}$ or $R'_{(5)}$. On the other catalyst models, however, the activation barriers for N_2 formation are comparable to those obtained for NO dissociation, slightly lower on Pt_{10} and Pt_{13} clusters, higher on Pt_{38} model, and nearly the same on Pt(111) surface (Table 2), this last value being in excellent agreement with previous reports.[41,44] However, in contrast to NO dissociation, the N_2 formation step is clearly exothermic for all catalyst models considered (Table 3).

It should be noted at this point that all the discussion is based on electronic energies, which are expected to describe correctly the bond-breaking and bond-forming steps investigated but do not include entropy effects nor dispersion interactions. To check the influence of these two factors, Gibbs free energies at 200 K and dispersion corrections using the Grimme's method have been calculated for the main steps of the mechanism on the most relevant Pt_{13}, Pt_{38}, and Pt(111) models, and the values are summarized in Tables S1−S3 in the Supporting Information. The Gibbs free energy values obtained for Pt_{13} and Pt_{38} models differ by less than 1 kcal mol^{-1} from the electronic energies discussed in the manuscript, and this difference remains below 2 kcal mol^{-1} on the Pt(111) surface. This small difference is not surprising taking into account the low reaction temperature studied and therefore the low values of the RT and TS terms. Dispersion corrections lead to slightly larger changes in the relative electronic and Gibbs free energies, but still in the 0−5 kcal mol^{-1} range except in a few particular cases in which the reaction involves desorption of atoms from the particle. None of these changes modify the trends and conclusions obtained, supporting our initial assumption that electronic energies describe correctly the reactivity of Pt clusters and particles.

Taking into account the experimentally observed delay in the production of $^{15}N_2$ on the Pt-CL sample (see the catalytic results presented in Figure S1), and the fact that gas-phase production of $^{15}N_2$ is below the stoichiometric value, it seems that N_2 recombination and desorption is the rate-determining step of the global process. To prove that point, we carried out a N_2-desorption experiment with the Pt-CL sample. First, the Pt-CL sample was exposed to ^{15}NO at 140 K for 30 min, then evacuated at 10^{-5} mbar, and annealed in vacuum up to 213 K. Afterward, the Pt-CL sample was again cooled down to 140 K and exposed to an Argon flow. Then, the temperature was gradually increased with a rate of 2 K min^{-1} and gas-phase species were analyzed by mass spectrometry. As shown in Figure 6, $^{15}N_2$ evolution was observed at 240 K, indicating that

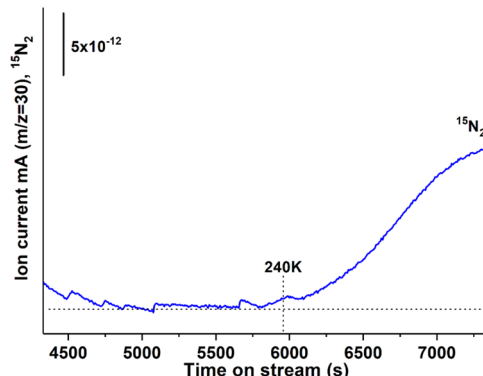a slow N_2 recombination should be responsible for the observed delay in the $^{15}N_2$ production on the Pt-CL sample.

Figure 6. $^{15}N_2$ desorption in the Pt-CL sample after being exposed to ^{15}NO at 140 K for 30 min, evacuated at 10^{-5} mbar, and annealed under vacuum up to 213 K, was again cooled down to 140 K and exposed to an argon flow.

According to the pathway proposed by DFT, it is key to force N atoms to become closer in order to recombine into N_2, and a possible way to achieve that is increasing the surface coverage of adsorbed N* species. To check this point, additional calculations were performed for step (5) on Pt_{13}, Pt_{38}, and Pt(111) catalyst models with a higher N* coverage (Figure S20). As expected, the presence of other N species adsorbed close to the N atoms on the Pt catalysts forces them to leave the stable 3-fold positions and approach to each other, leading to a significant decrease in the calculated activation energies and to a clear enhancement of the exothermicity of the process (see Tables 2 and 3).

To further confirm this hypothesis, another experiment was performed in our coupled IR-MS system in which the CO + NO reaction was carried out on the Pt-CL sample at 200 K with an increased total pressure from 1.4 to 2.2 mbar and modified $^{13}CO/^{15}NO$ molar ratio in the feed gas. Increasing the total pressure should enhance $^{15}N_2$ desorption from Pt clusters, thus leaving more Pt sites available for ^{15}NO adsorption and dissociation, with a corresponding promotion effect on the catalytic activity. In addition, modifying the $^{13}CO/^{15}NO$ molar ratio may influence the reaction rates for other elementary steps, including the NO dissociation, reaction between O and CO, and the N* recombination reaction to N_2. As shown in Table 4 and Figure S21, by increasing the total pressure from 1.4 to ∼2.2 mbar, both $^{13}CO_2$ formation and $^{15}N_2$ desorption are enhanced. On the other hand, increasing the ^{13}CO partial pressure enhances $^{15}N_2$ desorption and also promotes accordingly the production of $^{13}CO_2$ despite the lower ^{15}NO partial pressure. These results indicate that adsorbed N* species on the surface of Pt clusters may suppress the catalytic activity of the Pt-CL catalyst. In other words, the recombination of adsorb N* species is a key step in the low-temperature CO + NO reaction. Therefore, a maxima $^{13}CO_2$ formation rate was obtained at a $^{13}CO/^{15}NO$ molar ratio of ∼3.

Because the catalyst surface becomes covered by atomic N in the first stage of the CO + NO reaction, we have considered the possibility that adsorbed N atoms could react with CO yielding NCO (see eq 7) or with NO to produce N_2O (see eq 8) (see the optimized structures involved in these steps in

Table 4. Influence of Varying the Total Pressure from 1.4 to ~2.2 mbar and the $^{13}CO/^{15}NO$ Molar Ratio on the $^{13}CO_2$ and $^{15}N_2$ Production in the Pt-CL Sample at 200 K

total pressure	^{13}CO mbar	^{15}NO mbar	$^{13}CO/^{15}NO$ molar ratio	$^{13}CO_2$ formation $(10 \times 5)^a$ $mol_{CO_2}s^{-1}$ $molPt^{-1}$	$^{15}N_2$ formation $(10 \times 5)^a$ $mol_{N_2}s^{-1}$ $molPt^{-1}$
1.4	0.7	0.7	1	5	0
2.22	0.3	1.92	0.15	0	0
2.28	0.63	1.65	0.38	10.6	4.3
2.18	1.11	1.07	1.03	24.1	5.8
2.05	1.5	0.55	2.75	32.8	8.5

^{a}Activity measured at 250 s of reaction time.

Figures 5, S22 and S23). The activation energies for the reaction of CO with adsorbed N atoms are 15−20 kcal mol^{-1} higher than those previously reported for the reaction of CO with adsorbed O yielding CO_2 (Table 2), and the reaction energies are positive in all the cases (Table 3), suggesting that formation of NCO will only occur in the absence of atomic O on the catalyst surface. In contrast, comparison of the activation and reaction energies obtained for NO reaction with N atoms with those calculated for NO dissociation according to eq 3 suggests that N_2O formation will be competitive on all the Pt cluster models containing adsorbed N*. In fact, N_2O is observed in the operando IR study on all samples.

N_2O formed on the Pt clusters could further react with CO producing CO_2 according to eq 9. The process occurs, over all Pt cluster models, through a similar cyclic transition state in which the O atom of N_2O attacks the CO carbon atom bonded to one Pt site, while the terminal N atom of N_2O is attached to an adjacent Pt atom (Figure S24). The activation energies, around 30 kcal mol^{-1}, are only slightly higher than those involved in the formation of N_2O, and the step is clearly exothermic for all clusters with different sizes. Thus, the pathway involving the formation of N_2O according to (8) and its subsequent reaction with CO as described by (9) could also contribute to the overall reaction.

Therefore, according to DFT calculations, it can be concluded that single atoms, very small clusters, and too large nanoparticles cannot dissociate the NO molecule either mono-molecularly (3) or by direct reaction with CO (6), whereas medium-sized clusters can, with the monomolecular pathway being preferred. In addition, for the active medium-sized clusters, it is found that the rate-determining step of the CO + NO reaction is the formation of N_2 via recombination of the adsorbed N* atoms produced in the dissociation of NO (5) and that N_2O formation (8) and its reaction with CO (9) is competitive and might also contribute to the global reaction. All of these conclusions are consistent with the experimental results previously presented.

CONCLUSIONS

We have shown that, CO + NO reaction to produce CO_2 and N_2 can occur on stabilized subnanometric Pt clusters at a low temperature as low as 140 K. Then, combining operando IR spectroscopy experiments and DFT calculations, we have studied the low-temperature CO + NO reaction on different types of Pt species from single Pt atoms to subnanometric Pt clusters and nanoparticles. A reaction mechanism involving NO dissociation, CO oxidation by O*, and N* recombination followed by N_2 desorption has been proposed. NO dissociation takes place on both Pt clusters and nanoparticles while it is not favored on Pt atoms. Singly dispersed Pt atoms are not stable

under reaction conditions and agglomerate into Pt clusters. Because of their different redox properties, the oxidized Pt species in the Pt-CL sample can be reduced by CO to produce CO_2. In the case of Pt-NP, the oxidation of CO to CO_2 occurs in a much lower extension because of the strong interaction of Pt with CO and NO that remain adsorbed on the nanoparticles. Altogether, only Pt clusters allow NO dissociation and CO oxidation to occur well on the surface, while CO interaction is weak enough to avoid catalyst poisoning, resulting in enhanced catalytic performance. Because of the different interaction of the single atoms, clusters and nanoparticles with the reactions (CO and NO), subnanometric Pt clusters exhibit the best catalytic performance for low-temperature CO + NO reaction, being one example showing how the unique electronic and geometric structures of subnanometric metal clusters lead to remarkable catalytic properties compared to the corresponding single atoms and nanoparticles.

■ EXPERIMENTAL SECTION

Catalyst Synthesis and Characterization. The Pt-SA sample was prepared according to the method reported in the literature.[12] Pure-silica MCM-22 (0.97 g) was dried in an oven at 135 °C for 4 h. Trimethyl(methylcyclopentadienyl)-platinum(IV) (26 mg) was dissolved in 26 mL of pentane and then mixed with the dried pure-silica MCM-22 powder. After being stirred for 2 h at room temperature, the solid sample was separated by filtration and washed with pentane. The resultant solid sample was kept in a sealed vial. The loading of Pt in the Pt-SA sample was 0.20 wt %, determined by inductively coupled plasma (ICP).

The Pt-CL sample was prepared according to our previous work.[19] Subnanometric Pt clusters were introduced to pure-silica MCM-22 zeolite during the transformation of two-dimensional pure-silica ITQ-1 into three-dimensional MCM-22 zeolite. The loading of Pt is 0.10 wt %, determined by ICP.

The Pt-NP sample was prepared by conventional wetness impregnation. MCM-41 (pure silica, supplied by Sigma-Aldrich) (1.0 g) was dispersed in the aqueous solution of H_2PtCl_6. After the removal of water at 110 °C, the solid product was reduced by H_2 first at 200 °C for 2 h and then at 500 °C for 3 h. The loading of Pt in the Pt-NP sample was 0.85 wt %, determined by ICP.

The particle size distribution of three Pt samples was studied by electron microscopy. Samples for electron microscopy studies were prepared by dropping the suspension of the solid sample using ethanol as the solvent directly onto holey-carbon-coated Cu grids. The measurements were performed in a JEOL 2100F microscope operating at 200 kV both in transmission (TEM) and STEM. STEM images were obtained using a HAADF detector (HAADF), which allows Z-contrast imaging.

High-resolution STEM measurement was performed on a FEI Titan low-base microscope at 300 kV equipped with a Cs probe corrector, a monochromator, and an ultrabright X-FEG electron source. The convergence angle was 25 mrad and the inner and outer angles for HAADF imaging were 70 and 200 mrad, respectively. Control experiments have been performed and it was found that, under our experimental conditions, the subnanometric Pt species remain stable under the electron beam in the first several acquisitions.

Operando IR Studies. An Infrared catalytic cell (home-made) connected by a 1/16 capillary to a Balzer mass spectrometer has been used for the operando IR-MS studies. The IR cell is connected to a vacuum system with gas dosing facilities and allows in situ treatment in controlled atmospheres and temperatures from 103 to 773 K. For the IR study, ~10 mg of the sample was pressed into a thin pellet and located inside the IR cell. Pt-NP were activated in situ under H_2 flow at 350 °C for 1 h followed by vacuum treatment ($\sim 10^{-5}$ mbar) at the same temperature for 45 min. Pt-CL and Pt-SA were in situ activated under vacuum ($\sim 10^{-5}$ mbar) at 250 °C for 1.5 h. After activation, the sample temperature was decreased to the reaction temperature (140 and 200 K) under vacuum. Once achieved the reaction temperature, the sample is exposed to a continuous flow of $^{13}CO + ^{15}NO$ (1:1 molar ratio) at a rate of 0.1 mmol/h. The pressure in the catalytic IR cell was constant during the time of the experiment that settled to 1.4 mbar. Additional experiments were performed at higher reaction pressures, that is, ~2.2 mbar and varying the $^{13}CO/^{15}NO$ molar ratio from 0.36 to 2.75. The reaction products were followed by on line mass spectrometry in the multi-ion mode following the subsequent m/z fragmentation values, that is, 29 (^{13}CO), 31 (^{15}NO), 45 ($^{13}CO_2$), 30 ($^{15}N_2$), 47 ($^{15}N_2O$), 76 ($^{15}N_2O_3$), 94 ($^{15}N_2O_4$), 47 ($^{15}NO_2$). Blank experiments were done under similar reaction conditions in absence of the catalyst, resulting in no catalytic activity. For quantitative analysis, the value of each m/z mass was corrected taking into consideration the contribution of the rest of the products to the selected fragmentation and converted from mA to mol according to the calibration done for each product.

Computational Details. All calculations in this work are based on the periodic DFT and were carried out using the Perdew–Wang (PW91) functional[45] as implemented in the Vienna Ab-initio Simulation Package (VASP).[46,47] The valence density was expanded in a plane wave basis set with a kinetic energy cutoff of 500 eV, and the effect of the core electrons in the valence density was taken into account by means of the projected augmented wave formalism.[48] The Pt(111) surface was simulated by means of a 3 × 3 supercell slab model consisting of 45 Pt atoms arranged in five atomic layers and separated by a vacuum region of 15 Å to avoid interaction between periodically repeated slabs. Integration in the reciprocal space was carried out using a 3 × 3 × 1 mesh of Monkhorst–Pack[49] k-points, and during the geometry optimizations, the positions of the adsorbates and of the Pt atoms of the two uppermost layers were allowed to fully relax. The Pt_4, Pt_{10}, Pt_{13}, and Pt_{38} cluster models, as well as the reactant and product molecules, were placed in a 20 × 20 × 20 Å^3 cubic box, large enough to avoid spurious interactions between periodically repeated systems. Integration in the reciprocal space was carried out at the Γ k-point of the Brillouin zone, and the positions of all the atoms in these systems were fully optimized without any restriction. Finally, the Pt single atoms in MCM-22 were modeled by placing a Pt

atom in the large cage of a pure silica model of the MWW crystalline structure, with lattice parameters $a = b = 14.390$ and $c = 25.198$ Å and containing 216 atoms in the conventional unit cell (72 T and 144 O). Integration in the reciprocal space was carried out at the Γ k-point of the Brillouin zone, and the positions of all the atoms in this model were fully optimized without restrictions.

All calculations are spin-polarized, and all stationary points were characterized by partial hessian frequency calculations in which the Pt atoms of the catalyst model were kept fixed. Transition states were located using the DIMER[50,51] or CI-NEB[52] algorithms. The jmol[53] and MOLDEN[54] programs were used to build and visualize the systems and their frequencies throughout the work. Dispersion corrections to the energies were evaluated using the D3 Grimme's method.[55,56] The absolute Gibbs free energies of all species are given by

$$G = E_{tot} + E_{ZPE} + E_{vib} - TS_{vib}$$

where E_{tot} is the electronic energy obtained from the DFT calculation, E_{ZPE} is the zero point energy correction, E_{vib} is the vibrational thermal energy contribution, and S_{vib} is the vibrational entropy. The vibrational contributions to the energy and entropy were calculated according to

$$E_{ZPE} = \sum_{i=1}^{3N-6} \frac{1}{2} h\nu_i$$

$$E_{vib} = R \sum_{i=1}^{3N-6} \frac{h\nu_i}{k_B(e^{h\nu_i/k_B T} - 1)}$$

$$S_{vib} = R \sum_{i=1}^{3N-6} \frac{h\nu_i}{k_B(e^{h\nu_i/k_B T} - 1)} - \ln(1 - e^{h\nu_i/k_B T})$$

using the vibrational frequencies ν obtained from the DFT calculations.

■ ASSOCIATED CONTENT

ⓢ Supporting Information

The Supporting Information is available free of charge on the ACS Publications website at DOI: 10.1021/acscatal.9b03207.

HR-STEM images of all catalyst samples after reaction, additional MS experiments and DFT optimized geometries of adsorbed CO and NO, and of the structures involved in the reaction mechanism on all catalyst models (PDF)

■ AUTHOR INFORMATION

Corresponding Author

*E-mail: acorma@itq.upv.es. Web: www.avelinocorma.com.

ORCID ⓘ

Mercedes Boronat: 0000-0002-6211-5888

Raul Arenal: 0000-0002-2071-9093

Patricia Concepcion: 0000-0003-2058-3103

Avelino Corma: 0000-0002-2232-3527

Author Contributions

⊥E.F. and L.L. authors contributed equally to this work.

Notes

The authors declare no competing financial interest.

REFERENCES

(1) Roduner, E. Size Matters: Why Nanomaterials Are Different. *Chem. Soc. Rev.* **2006**, *35*, 583−592.

(2) Liu, L.; Corma, A. Metal Catalysts for Heterogeneous Catalysis: From Single Atoms to Nanoclusters and Nanoparticles. *Chem. Rev.* **2018**, *118*, 4981−5079.

(3) Mason, M. G. Electronic Structure of Supported Small Metal Clusters. *Phys. Rev. B: Condens. Matter Mater. Phys.* **1983**, *27*, 748−762.

(4) Yoon, B.; Hakkinen, H.; Landman, U.; Worz, A. S.; Antonietti, J. M.; Abbet, S.; Judai, K.; Heiz, U. Charging Effects on Bonding and Catalyzed Oxidation of CO on Au$_8$ Clusters on MgO. *Science* **2005**, *307*, 403−407.

(5) Herzing, A. A.; Kiely, C. J.; Carley, A. F.; Landon, P.; Hutchings, G. J. Identification of Active Gold Nanoclusters on Iron Oxide Supports for CO Oxidation. *Science* **2008**, *321*, 1331−1335.

(6) Corma, A.; Concepción, P.; Boronat, M.; Sabater, M. J.; Navas, J.; Yacaman, M. J.; Larios, E.; Posadas, A.; López-Quintela, M. A.; Buceta, D.; Mendoza, E.; Guilera, G.; Mayoral, A. Exceptional Oxidation Activity with Size-Controlled Supported Gold Clusters of Low Atomicity. *Nat. Chem.* **2013**, *5*, 775−781.

(7) Oliver-Meseguer, J.; Cabrero-Antonino, J. R.; Dominguez, I.; Leyva-Perez, A.; Corma, A. Small Gold Clusters Formed in Solution Give Reaction Turnover Numbers of 10^7 at Room Temperature. *Science* **2012**, *338*, 1452−1455.

(8) Lei, Y.; Mehmood, F.; Lee, S.; Greeley, J.; Lee, B.; Seifert, S.; Winans, R. E.; Elam, J. W.; Meyer, R. J.; Redfern, P. C.; Teschner, D.; Schlogl, R.; Pellin, M. J.; Curtiss, L. A.; Vajda, S. Increased Silver Activity for Direct Propylene Epoxidation via Subnanometer Size Effects. *Science* **2010**, *328*, 224−228.

(9) Liu, C.; Yang, B.; Tyo, E.; Seifert, S.; DeBartolo, J.; von Issendorff, B.; Zapol, P.; Vajda, S.; Curtiss, L. A. Carbon Dioxide Conversion to Methanol over Size-Selected Cu$_4$ Clusters at Low Pressures. *J. Am. Chem. Soc.* **2015**, *137*, 8676−8679.

(10) Hirabayashi, S.; Ichihashi, M. Catalytic oxidation of CO with N$_2$O on isolated copper cluster anions. *Phys. Chem. Chem. Phys.* **2014**, *16*, 26500−26505.

(11) Vajda, S.; Pellin, M. J.; Greeley, J. P.; Marshall, C. L.; Curtiss, L. A.; Ballentine, G. A.; Elam, J. W.; Catillon-Mucherie, S.; Redfern, P. C.; Mehmood, F.; Zapol, P. Subnanometre Platinum Clusters as Highly Active and Selective Catalysts for the Oxidative Dehydrogenation of Propane. *Nat. Mater.* **2009**, *8*, 213−216.

(12) Ding, K.; Gulec, A.; Johnson, A. M.; Schweitzer, N. M.; Stucky, G. D.; Marks, L. D.; Stair, P. C. Identification of Active Sites in CO Oxidation and Water-Gas Shift over Supported Pt Catalysts. *Science* **2015**, *350*, 189−192.

(13) Zhai, Y.; Pierre, D.; Si, R.; Deng, W.; Ferrin, P.; Nilekar, A. U.; Peng, G.; Herron, J. A.; Bell, D. C.; Saltsburg, H.; Mavrikakis, M.; Flytzani-Stephanopoulos, M. Alkali-Stabilized Pt-OH$_x$ Species Catalyze Low-Temperature Water-Gas Shift Reactions. *Science* **2010**, *329*, 1633−1636.

(14) Wörz, A. S.; Judai, K.; Abbet, S.; Heiz, U. Cluster Size-Dependent Mechanisms of the CO+NO Reaction on Small Pd$_n$ (n≤30) Clusters on Oxide Surfaces. *J. Am. Chem. Soc.* **2003**, *125*, 7964−7970.

(15) Judai, K.; Abbet, S.; Wörz, A. S.; Heiz, U.; Henry, C. R. Low-Temperature Cluster Catalysis. *J. Am. Chem. Soc.* **2004**, *126*, 2732−2737.

(16) Boronat, M.; Corma, A. Oxygen Activation on Gold Nanoparticles: Separating the Influence of Particle Size, Particle Shape and Support Interaction. *Dalton Trans.* **2010**, *39*, 8538−8546.

(17) Rodriguez, J. A.; Senanayake, S. D.; Stacchiola, D.; Liu, P.; Hrbek, J. The Activation of Gold and the Water-Gas Shift Reaction: Insights from Studies with Model Catalysts. *Acc. Chem. Res.* **2014**, *47*, 773−782.

(18) Rodriguez, J. A.; Grinter, D. C.; Liu, Z.; Palomino, R. M.; Senanayake, S. D. Ceria-Based Model Catalysts: Fundamental Studies on the Importance of the Metal-Ceria Interface in CO Oxidation, the Water-Gas Shift, CO$_2$ Hydrogenation, and Methane and Alcohol Reforming. *Chem. Soc. Rev.* **2017**, *46*, 1824−1841.

(19) Liu, L.; Díaz, U.; Arenal, R.; Agostini, G.; Concepción, P.; Corma, A. Generation of Subnanometric Platinum with High Stability during Transformation of a 2D Zeolite into 3D. *Nat. Mater.* **2017**, *16*, 132−138.

(20) Liu, L.; Arenal, R.; Meira, D. M.; Corma, A. Generation of Gold Nanoclusters Encapsulated in an MCM-22 Zeolite for the Aerobic Oxidation of Cyclohexane. *Chem. Commun.* **2019**, *55*, 1607−1610.

(21) Liu, L.; Zakharov, D. N.; Arenal, R.; Concepcion, P.; Stach, E. A.; Corma, A. Evolution and Stabilization of Subnanometric Metal Species in Confined Space by in situ TEM. *Nat. Commun.* **2018**, *9*, 574.

(22) Bera, P.; Patil, K. C.; Jayaram, V.; Subbanna, G. N.; Hegde, M. S. Ionic Dispersion of Pt and Pd on CeO$_2$ by Combustion Method: Effect of Metal−Ceria Interaction on Catalytic Activities for NO Reduction and CO and Hydrocarbon Oxidation. *J. Catal.* **2000**, *196*, 293−301.

(23) Hu, Y.; Griffiths, K.; Norton, P. R. Surface Science Studies of Selective Catalytic Reduction of NO: Progress in the Last Ten Years. *Surf. Sci.* **2009**, *603*, 1740−1750.

(24) Leonowicz, M. E.; Lawton, J. A.; Lawton, S. L.; Rubin, M. K. MCM-22: A Molecular Sieve with Two Independent Multidimensional Channel Systems. *Science* **1994**, *264*, 1910−1913.

(25) Hadjiivanov, K. I. Identification of Neutral and Charged N$_x$O$_y$ Surface Species by IR Spectroscopy. *Catal. Rev.* **2000**, *42*, 71−144.

(26) Maestri, M.; Iglesia, E. First-Principles Theoretical Assessment of Catalysis by Confinement: NO-O$_2$ Reactions within Voids of Molecular Dimensions in Siliceous Crystalline Frameworks. *Phys. Chem. Chem. Phys.* **2018**, *20*, 15725−15735.

(27) Li, G.-J.; Fujimoto, T.; Fukuoka, A.; Ichikawa, M. EXAFS and Fourier Transform IR Characterization of Platinum Carbonyl Clusters $[Pt_3(CO)_6]_n^{2−}$ (n=3,4) Encapsulated in NaY Zeolites and Their Effective Catalysis in the CO + NO Reaction. *J. Chem. Soc., Chem. Commun.* **1991**, 1337−1339.

(28) Andonova, S.; Ok, Z. A.; Drenchev, N.; Ozensoy, E.; Hadjiivanov, K. Pt/CeO$_x$/ZrO$_x$/γ-Al$_2$O$_3$ Ternary Mixed Oxide DeNOx Catalyst: Surface Chemistry and NO$_x$ Interactions. *J. Phys. Chem. C* **2018**, *122*, 12850−12863.

(29) Xiao, P.; Davis, R. C.; Ouyang, X.; Li, J.; Thomas, A.; Scott, S. L.; Zhu, J. Mechanism of NO Reduction by CO over Pt/SBA-15. *Catal. Commun.* **2014**, *50*, 69−72.

(30) Freysz, J.-L.; Saussey, J.; Lavalley, J.-C.; Bourges, P. In Situ FTIR Study of the NO+CO Reaction on a Silica-Supported Platinum Catalyst at Atmospheric Pressure Using a New Pulse Technique. *J. Catal.* **2001**, *197*, 131−138.

(31) Park, J. B.; Ratliff, J. S.; Ma, S.; Chen, D. A. Understanding the Reactivity of Oxide-Supported Bimetallic Clusters: Reaction of NO with CO on TiO₂(110)-Supported Pt−Rh Clusters. *J. Phys. Chem. C* **2007**, *111*, 2165−2176.

(32) Backus, E. H. G.; Eichler, A.; Grecea, M. L.; Kleyn, A. W.; Bonn, M. Adsorption and Dissociation of NO on Stepped Pt (533). *J. Chem. Phys.* **2004**, *121*, 7946−7954.

(33) Dobrin, S. CO Oxidation on Pt Nanoclusters, Size and Coverage Effects: a Density Functional Theory Study. *Phys. Chem. Chem. Phys.* **2012**, *14*, 12122−12129.

(34) Peng, G.; Mavrikakis, M. Adsorbate Diffusion on Transition Metal Nanoparticles. *Nano Lett.* **2015**, *15*, 629−634.

(35) Verga, L. G.; Russell, A. E.; Skylaris, C. K. Ethanol, O, and CO Adsorption on Pt Nanoparticles: Effects of Nanoparticle Size and Graphene Support. *Phys. Chem. Chem. Phys.* **2018**, *20*, 25918−25930.

(36) Chaves, A. S.; Piotrowski, M. J.; Guedes-Sobrinho, D.; Da Silva, J. L. F. Theoretical Investigation of the Adsorption Properties of CO, NO, and OH on Monometallic and Bimetallic 13-Atom Clusters: The Example of Cu13, Pt7Cu6, and Pt13. *J. Phys. Chem. A* **2015**, *119*, 11565−11573.

(37) Ge, Q.; Neurock, M. Structure Dependence of NO Adsorption and Dissociation on Platinum Surfaces. *J. Am. Chem. Soc.* **2004**, *126*, 1551−1559.

(38) Deshlahra, P.; Conway, J.; Wolf, E. E.; Schneider, W. F. Influence of Dipole-Dipole Interactions on Coverage-Dependent Adsorption: CO and NO on Pt(111). *Langmuir* **2012**, *28*, 8408−8417.

(39) Huang, X.; Mason, S. E. DFT-GGA Errors in NO Chemisorption Energies on (111) Transition Metal Surfaces. *Surf. Sci.* **2014**, *621*, 23−30.

(40) Hamad, B.; El-Bayyari, Z.; Marashdeh, A. Investigation of the Stability of Platinum Clusters and the Adsorption of Nitrogen Monoxide: First Principles Calculations. *Chem. Phys.* **2014**, *443*, 26−32.

(41) Gonzalez, J. D.; Shojaee, K.; Haynes, B. S.; Montoya, A. The Effect of Surface Coverage on N₂, NO and N₂O Formation over Pt(111). *Phys. Chem. Chem. Phys.* **2018**, *20*, 25314−25323.

(42) Han, B. C.; Miranda, C. R.; Ceder, G. Effect of Particle Size and Surface Structure on Adsorption of O and OH on Platinum Nanoparticles: A First-Principles Study. *Phys. Rev. B: Condens. Matter Mater. Phys.* **2008**, *77*, 075410.

(43) Verga, L. G.; Aarons, J.; Sarwar, M.; Thompsett, D.; Russell, A. E.; Skylaris, C.-K. DFT Calculation of Oxygen Adsorption on Platinum Nanoparticles: Coverage and Size Effects. *Faraday Discuss.* **2018**, *208*, 497−522.

(44) Ma, H.; Schneider, W. F. Structure- and Temperature-Dependence of Pt-Catalyzed Ammonia Oxidation Rates and Selectivities. *ACS Catal.* **2019**, *9*, 2407−2414.

(45) Perdew, J. P.; Wang, Y. Accurate and Simple Analytic Representation of the Electron-Gas Correlation Energy. *Phys. Rev. B: Condens. Matter Mater. Phys.* **1992**, *45*, 13244−13249.

(46) Kresse, G.; Furthmüller, J. Efficient iterative schemes forab initiototal-energy calculations using a plane-wave basis set. *Phys. Rev. B: Condens. Matter Mater. Phys.* **1996**, *54*, 11169−11186.

(47) Kresse, G.; Joubert, D. From Ultrasoft Pseudopotentials to the Projector Augmented-Wave Method. *Phys. Rev. B: Condens. Matter Mater. Phys.* **1999**, *59*, 1758−1775.

(48) Blöchl, P. E. Projector Augmented-Wave Method. *Phys. Rev. B: Condens. Matter Mater. Phys.* **1994**, *50*, 17953−17979.

(49) Monkhorst, H. J.; Pack, J. D. Special Points for Brillouin-Zone Integrations. *Phys. Rev. B: Condens. Matter Mater. Phys.* **1976**, *13*, 5188−5192.

(50) Henkelman, G.; Jónsson, H. A Dimer Method for Finding Saddle Points on High Dimensional Potential Surfaces Using only First Derivatives. *J. Chem. Phys.* **1999**, *111*, 7010−7022.

(51) Heyden, A.; Bell, A. T.; Keil, F. J. Efficient Methods for Finding Transition States in Chemical Reactions: Comparison of Improved Dimer Method and Partitioned Rational Function Optimization Method. *J. Chem. Phys.* **2005**, *123*, 224101.

(52) Henkelman, G.; Uberuaga, B. P.; Jónsson, H. A Climbing Image Nudged Elastic Band Method for Finding Saddle Points and Minimum Energy Paths. *J. Chem. Phys.* **2000**, *113*, 9901−9904.

(53) http://www.jmol.org/.

(54) Schaftenaar, G.; Noordik, J. H. Molden: A Pre- and Post-Processing Program for Molecular and Electronic Structures. *J. Comput.-Aided Mol. Des.* **2000**, *14*, 123−134.

(55) Grimme, S. Accurate Description of Van der Waals Complexes by Density Functional Theory Including Empirical Corrections. *J. Comput. Chem.* **2004**, *25*, 1463−1473.

(56) Grimme, S. Semiempirical GGA-type Density Functional Constructed with a Long-Range Dispersion Correction. *J. Comput. Chem.* **2006**, *27*, 1787−1799.